buildings

MDPI

Article

Experimental and Analytical Study of a Segmented Buckling Restrained Brace

Shuai Xu [1,2,*], Yuchao Yin [1], Yanyan Liu [3], Xiuli Wang [1], Wei Wang [1] and Yan Li [1]

[1] School of Civil Engineering, Jilin Jianzhu University, Changchun 130118, China; yinyuchao@student.jlju.edu.cn (Y.Y.)
[2] Key Laboratory of Architectural Cold Climate Energy Management, Ministry of Education, Jilin Jianzhu University, Changchun 130118, China
[3] National Engineering Research Center of Biomaterials, Nanjing Forestry University, Nanjing 210037, China; liuyanyan@njfu.edu.cn
* Correspondence: xushuai@jlju.edu.cn; Tel.: +86-18686630781

Abstract

Buckling-restrained braces (BRBs) are widely recognized as effective energy-dissipation components that enhance the seismic resilience of structures. This study introduces a segmented buckling-restrained brace (S-BRB), composed of a Q235 steel core plate, restraining members, limiting plates, and bolts. A prototype S-BRB was designed, fabricated, and tested under quasi-static loading to investigate its failure mechanisms and hysteretic behavior. A corresponding numerical model was developed in ABAQUS to further evaluate its seismic performance. Test results demonstrate that the limiting plates effectively restrict the deformation of each core plate segment, enabling progressive yielding and preventing premature fracture at weaker sections. The S-BRB exhibited stable hysteretic loops, excellent energy-dissipation capacity, and strong deformation ability. Overall, the S-BRB shows reliable seismic behavior and adaptability in design, indicating strong potential for meeting practical seismic performance requirements.

Keywords: segmented buckling-restrained brace; quasi-static tests; hysteretic properties

Academic Editor: Eric M. Lui

Received: 26 August 2025
Revised: 27 September 2025
Accepted: 30 September 2025
Published: 2 October 2025

Citation: Xu, S.; Yin, Y.; Liu, Y.; Wang, X.; Wang, W.; Li, Y. Experimental and Analytical Study of a Segmented Buckling Restrained Brace. *Buildings* **2025**, *15*, 3564. https://doi.org/10.3390/buildings15193564

1. Introduction

As architectural configurations grow increasingly intricate, structural systems are confronted with a series of challenges, among which diminished stability and insufficient seismic redundancy are the most pronounced [1–4]. Traditional structural braces components, in turn, are hard-pressed to strike an adequate balance between load-bearing capacity and energy-dissipation requirements [5–7]; by contrast, buckling-restrained braces exhibit remarkably stable and robust hysteretic curves under both tensile and compressive cyclic loading, thereby significantly enhancing the seismic resilience of the overall structure. Consequently, owing to their exceptional energy-dissipation capabilities, buckling-restrained braces have been widely adopted in the seismic design of building structures [8–10]. Furthermore, assembled buckling-restrained braces leverage prefabricated steel components and modular connection technologies, successfully overcoming the inherent limitations of traditional braces—namely, excessive self-weight, slow construction speed, and the inability to be repaired after an earthquake [11–15].

Research on prefabricated buckling-restrained braces (P-BRBs) has progressed in three main directions: material innovation, geometric design, and performance validation, leading to a clearer understanding of research gaps and future trends.

In terms of materials and member types, Kuwahara et al. [16] proposed a steel tube-based BRB filled with mortar for confinement. Genna [17] adopted flat steel cores with stiffened channel sections to achieve assembly-based design. Usami et al. [18] systematically investigated the performance of aluminum alloy BRBs under different restraint conditions through low-cycle fatigue tests. Hoveidae and Radpour [19] introduced an all-steel tube-in-tube configuration, while Zhou et al. [20] developed a perforated steel BRB, both aiming to enhance post-yield stiffness and reduce residual displacements.

Regarding geometric and assembly innovations, Jiang et al. [21] designed a double-rectangular-tube BRB with bolted connections for rapid on-site assembly. Jia et al. [22] proposed a fish-bone shaped all-steel BRB (FB-BRB), and Azizi et al. [23] developed a Y-shaped BRB (YHBRB), both utilizing multi-core or hybrid-yield strategies to improve seismic resilience. Hu et al. [24] addressed construction challenges in grout-filled BRBs by introducing segmental prefilled members and sleeve assemblies.

In performance evaluation and seismic applications, Ma et al. [25] conducted finite element simulations and full-scale tests to assess the effectiveness of external fractal-structured BRBs in strengthening multi-story frames. Takeuchi and Wada [26] summarized BRB design principles, experimental validation, and high-rise applications, emphasizing energy dissipation through core yielding. Shrif et al.'s [27] nonlinear time-history analysis of 24 BRB configurations showed that the center-bay C2 design most effectively reduced base shear and overturning moment. Shi et al. [6] reported a case study on a 24-story steel structure retrofitted with mid-span BRBs, demonstrating significantly improved lateral stiffness. Bagheri et al. [28] evaluate BRBs for seismic retrofitting of RC structures, using 3D modeling to assess their impact on resilience considering SSI and pounding effects.

Despite these advances, challenges remain in manufacturing complexity, insufficient lightweight restraint materials, and the lack of unified design codes. Future work should focus on simplifying fabrication, developing lightweight restraint systems, and establishing reliable design guidelines through systematic testing and numerical simulation to promote efficient and economical seismic solutions.

To address these limitations, this study proposes a segmented buckling-restrained brace (S-BRB) (Figure 1). This design eliminates the use of unbonded material in the manufacturing process, and the core plate is welded to limit plates [29,30]. The restraining members are formed by several steel channels connected to upper and lower restraining plates using high-strength bolts. Unlike traditional BRB designs, the S-BRB achieves segmented energy dissipation through an ingenious configuration of the core plate and limiting plates. In conventional BRBs, the core plate is prone to failure at its weakest point [31]. To mitigate this issue, two limiting plates are installed within the energy-dissipating sections of the core plate. These plates restrict the deformation of each section, enabling the core plate to yield progressively. This prevents deformation from concentrating in a single area, thereby fully utilising the energy-dissipating capacity of the entire core plate (Figure 2). Additionally, the lateral stiffeners and short stiffeners within the lateral restraining member further enhance its overall stiffness, preventing local instability and ensuring stable mechanical performance. The integrated structure of the restraining members provides stable lateral constraint forces to the core plate, effectively suppressing premature buckling and achieving segmented, gradual buckling energy dissipation. The fully bolted connection design also reduces the weight of individual components, facilitating easier transportation and installation, as well as simplifying replacement during post-earthquake repairs. By utilising conventional materials and providing a rational design basis, the S-BRB opens up opportunities for more widespread usage of BRBs, reducing the reliance on specialized design or fabrication. In this study, low-cycle cyclic loading tests and numerical analysis were conducted on the segmented buckling-restrained braces (S-BRB) to reveal their material

properties and hysteretic performance, investigate the energy dissipation mechanism of the core plate partition and the synergistic mechanism of the restraining member, and analyse the deformation and failure mechanisms of S-BRBs.

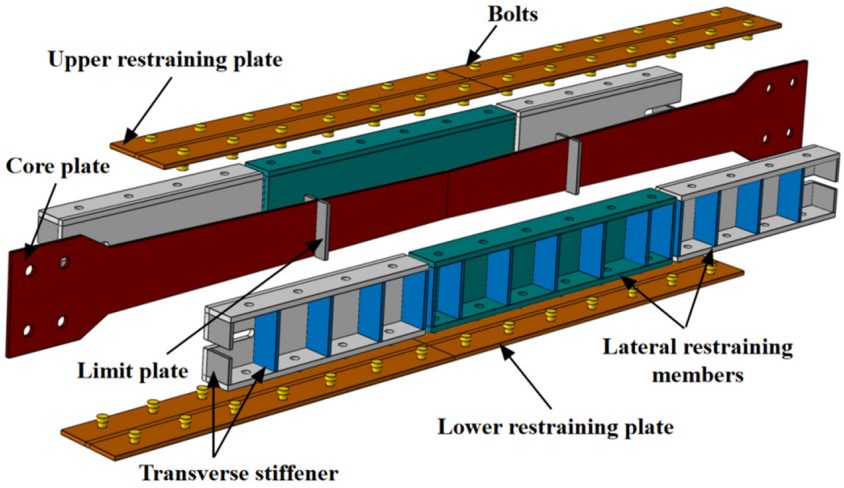

Figure 1. Schematic diagram of S-BRB.

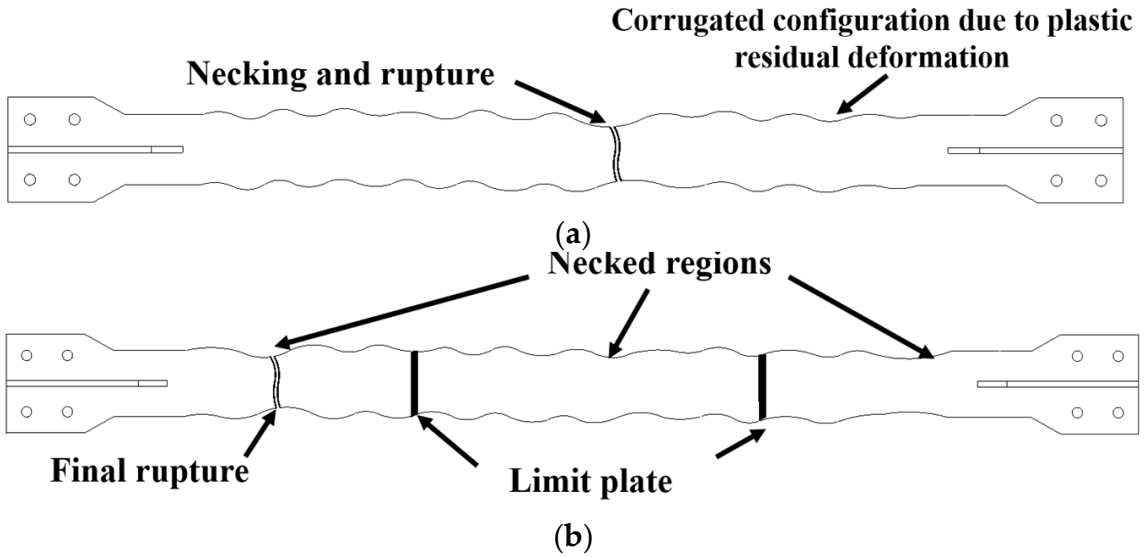

Figure 2. Expected deformation and rupture mechanisms of conventional and segmented buckling-restrained braces. (**a**) Conventional buckling-restrained brace; (**b**) Segmented buckling-restrained brace.

2. Design of S-BRB

The S-BRB core plate features a variable cross-section, being narrowest in the middle and wider towards both ends. This design ensures that the core plate yields first in its central region. It was assumed that when subjected to an axial force, the core plate would gradually exhibit a multi-wave instability mode as the load increased. To illustrate the change process of this multi-wave instability more clearly, an amplified schematic is presented in Figure 3, wherein the deformation of the lateral restraining members was ignored for simplicity.

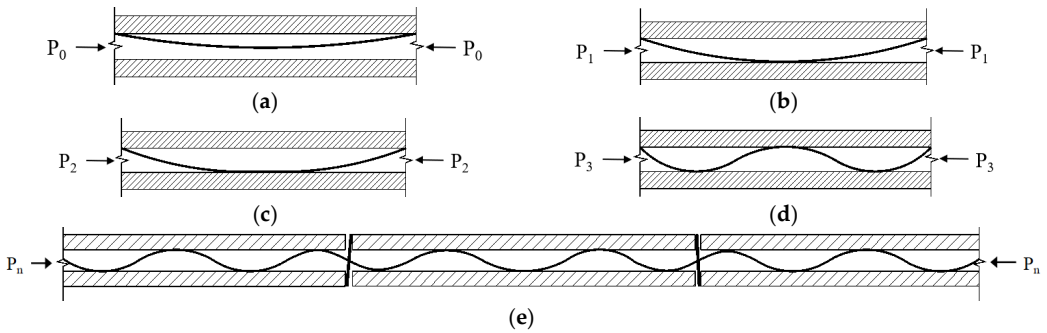

Figure 3. Development in high mode buckling within the yielding portion of core plate: (**a**) initial state; (**b**) one-point contact; (**c**) face-to-fact contact; (**d**) multiple-point contact; (**e**) final state.

Initially, a small initial deflection exists in the core plate due to inherent machining tolerances. Consequently, a sinusoidal half-wave flexural mode appears under a very small axial force (Figure 3a). As the load increases, the core plate makes contact with the lateral restraining members, which restrains its flexural deformation (Figure 3b). Subsequently, with a further gradual increase in load, the contact interface between the core plate and the lateral restraining members transitions from an initial point contact to a full-face contact (Figure 3c). Once this contact reaches a critical state, the deformation mode converts from the first-order to a third-order flexural mode (Figure 3d). The peak of the flexural core plate soon contacts the restraining members again, leading to renewed restraint of the deformation [32]. Thereby, the number of flexural half-waves gradually increases, expanding from the middle towards the ends of the core plate.

Throughout this multi-wave buckling process, the buckling mode transitions from low-order to high-order without causing an instantaneous reduction in bearing capacity. Because the middle section of the core plate has the smallest cross-sectional area, it enters plastic deformation first. At this stage, the limiting plate and lateral restraining members interact through mutual squeezing before ultimate failure, which restricts further plastic deformation in the middle section. This allows the core plate segments at both ends to continue dissipating energy until they eventually fail (Figure 3e).

In order to simplify the analysis, an isotropic core plate was analyzed according to the elastic-plastic buckling problem of a compression member through the tangent modulus theory.

In order to simplify the analysis, the isotropic core plate was treated as an elastic-plastic buckling problem for a compression member, analyzed through the tangent modulus theory. It was assumed that the local squeezing distributed forces acting on the middle and the end of the core plate's yielding section were $q_1(x)$ and $q_n(x)$, respectively. The buckling half-wave lengths for the middle and end segments of the yielding section were defined as L_1 and L_n, respectively, as shown in Figure 4.

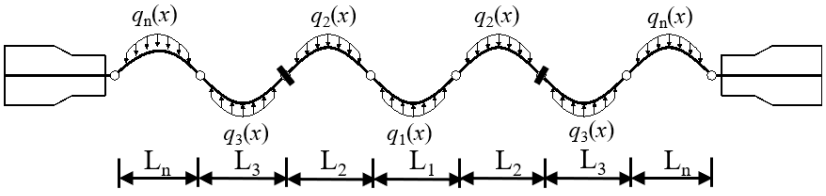

Figure 4. Simplified sketch of high mode buckling within the yielding portion of core plate.

For detailed investigation, a single flexural half-wave located at the mid-length of the yielding segment is isolated; this segment represents the state after yielding under compression and prior to ultimate failure. In this isolated segment, the frictional contact force on the mid-core plate is assumed to be negligibly small, as illustrated in Figure 5.

On the basis of the tangent-modulus theory, the analytical expression for the buckling half-wavelength can be written as follows [33]:

$$L_1 = \pi t_c \sqrt{\frac{E_t}{12\omega f_y}} = \pi t_c \sqrt{\frac{\alpha}{12\omega\epsilon_y}} \tag{1}$$

where t_c was the thickness of the core plate yielding section of the plate, f_y was the yield stress of the core plate, E_t was the tangent modulus of the core plate, α was the ratio of the tangent modulus E_t to the elastic modulus E, ε_y was the yield strain of the yield section of the core plate, ω was the tensile capacity adjustment factor of the BRB, and $\omega > 1$, the reinforcement after yielding was considered. Based on the balance of forces on both sides of the isolated body, Equations (2) and (3) were established, leading to the derivation of Equation (4) through their association.

$$2N\sin\theta = \int_{L_1} q_1(x)dx = Q_1 \tag{2}$$

$$N\cos\theta = \omega P_y \tag{3}$$

$$Q_1 = 2\omega tg\theta P_y \tag{4}$$

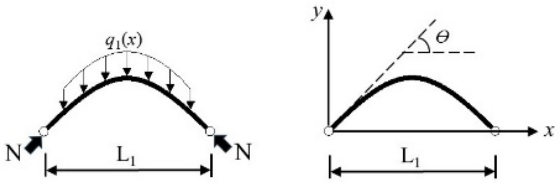

Figure 5. Isolated body mid-yielding portion of core plate.

Recognizing that the flexural waveform closely approximates a sinusoidal half-wave, the deflected shape is expressed analytically as:

$$y = \frac{c}{2}\sin\left(\frac{\pi x}{L_n}\right) \tag{5}$$

where c was the sum of the clearance between the core plate and the lateral restraining members.

The absolute value of the curve angle at position x = 0 can be obtained by differentiating Equation (5):

$$\theta = y'|_{x=0} = \frac{\pi c}{2L_1} \tag{6}$$

According to the small deformation assumption tgθ = θ, the force was obtained by substituting Equation (6) into Equation (4).

$$Q_1 = 2\omega\frac{\pi c}{2L_1}P_y = \pi\omega P_y\left(\frac{c}{L_1}\right) = \omega P_y\sqrt{\frac{12\omega\varepsilon_y}{\alpha}}\left(\frac{c}{t_c}\right) \tag{7}$$

The buckling half-wavelength of a constant-section core plate is distributed unevenly along its axial direction. Specifically, the half-wavelength in plate sections near the ends of the yield section is smaller than that in the intermediate region. This discrepancy results in greater local compressive stress from the lateral restraining members on the core plate at the ends compared to the middle. Consequently, local instability failure of the BRB is more likely to initiate at the ends of the yield section.

The S-BRB addresses this issue by employing a variable-section core plate, where the cross-sectional area decreases towards the centre. This design adjusts the buckling half-

wavelength along the plate, promoting a more balanced distribution of the compressive force that the core plate exerts on the lateral restraining members across the entire region. Furthermore, the installation of limiting plates on the core plate ensures that the central region does not fail prematurely due to excessive local buckling. This mechanism effectively prevents the entire BRB from undergoing catastrophic failure.

3. Test Program

3.1. Material

The core plate of the S-BRB is fabricated from Q235 steel. To evaluate the material properties of this core plate, a monotonic loading test was designed. This test involved three specimens, labeled Q1, Q2, and Q3, each with a length of 220 mm and a thickness of 6 mm, as illustrated in Figure 6. The uniaxial tensile test primarily utilized a Digital Image Correlation (DIC) measurement system for data acquisition, with the experiments conducted using a WAW-600kN microcomputer-controlled electro-hydraulic servo testing machine (Figure 7). To accurately capture the loading conditions of the specimens, a specific surface preparation was followed, as shown in Figure 8. First, a matte white primer was sprayed onto the specimen surfaces; subsequently, black paint was randomly applied to create a speckled pattern essential for DIC analysis.

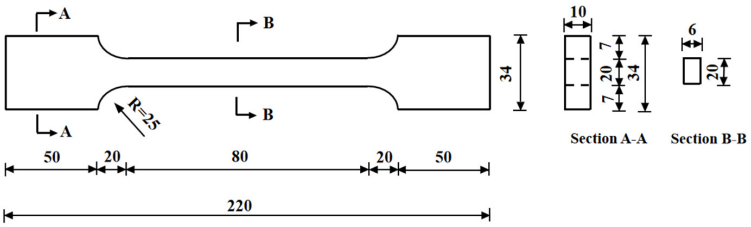

Figure 6. Dimensions of monotonic loading test specimen.

Figure 7. Test equipment: (**a**) Front view; (**b**) Side view.

(**a**) (**b**)

Figure 8. Test specimen. (**a**) Speckled pattern; (**b**) Fracture morphology after test.

Turning to the experimental observations, the stress–strain curves exhibited a pronounced yield plateau, thereby confirming the excellent ductility of Q235 steel, with an average elongation at fracture of approximately 25% (Figure 9). The tensile speckle images of the Q235 steel specimen captured by the DIC system immediately prior to fracture are presented in Figure 10. In these images, the scale values corresponding to 'eyy' represent the vertical strain under tensile loading, while the values for 'exx' indicate the horizontal strain. As the strain progressively increased from low to high values, the associated colours on the cloud map transitioned accordingly, from purple to red.

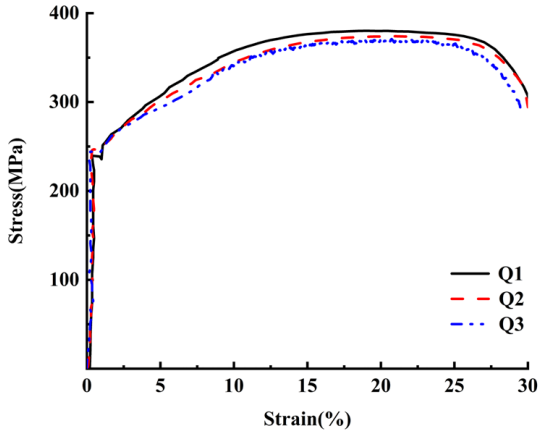

Figure 9. Stress–strain curves of specimens.

From the strain cloud map, it can be clearly observed that the necking region exhibits highly distinctive characteristics within a specific area of the specimen. Within this localized region, the specimen undergoes concentrated deformation, resulting in a significant strain gradient compared to the rest of the material. In contrast, the non-necking region displays a uniformly distributed strain cloud map with stable strain levels and no notable fluctuations. The strain intensity in the necking region is markedly higher than that in the non-necking region. Furthermore, as time progressed during the test, the equivalent strain in the necking region continued to rise, following an upward-trending curve, whereas in the non-necking region, the equivalent strain remained nearly unchanged from its initial state.

Overall analysis indicates that the specimen underwent uniform deformation initially, with the distribution of micro-strain regions in both the transverse and longitudinal directions being relatively even and showing minimal disparity. This indicates that the Q235 steel demonstrates excellent mechanical properties and stable, consistent deformation capabilities during tensile testing.

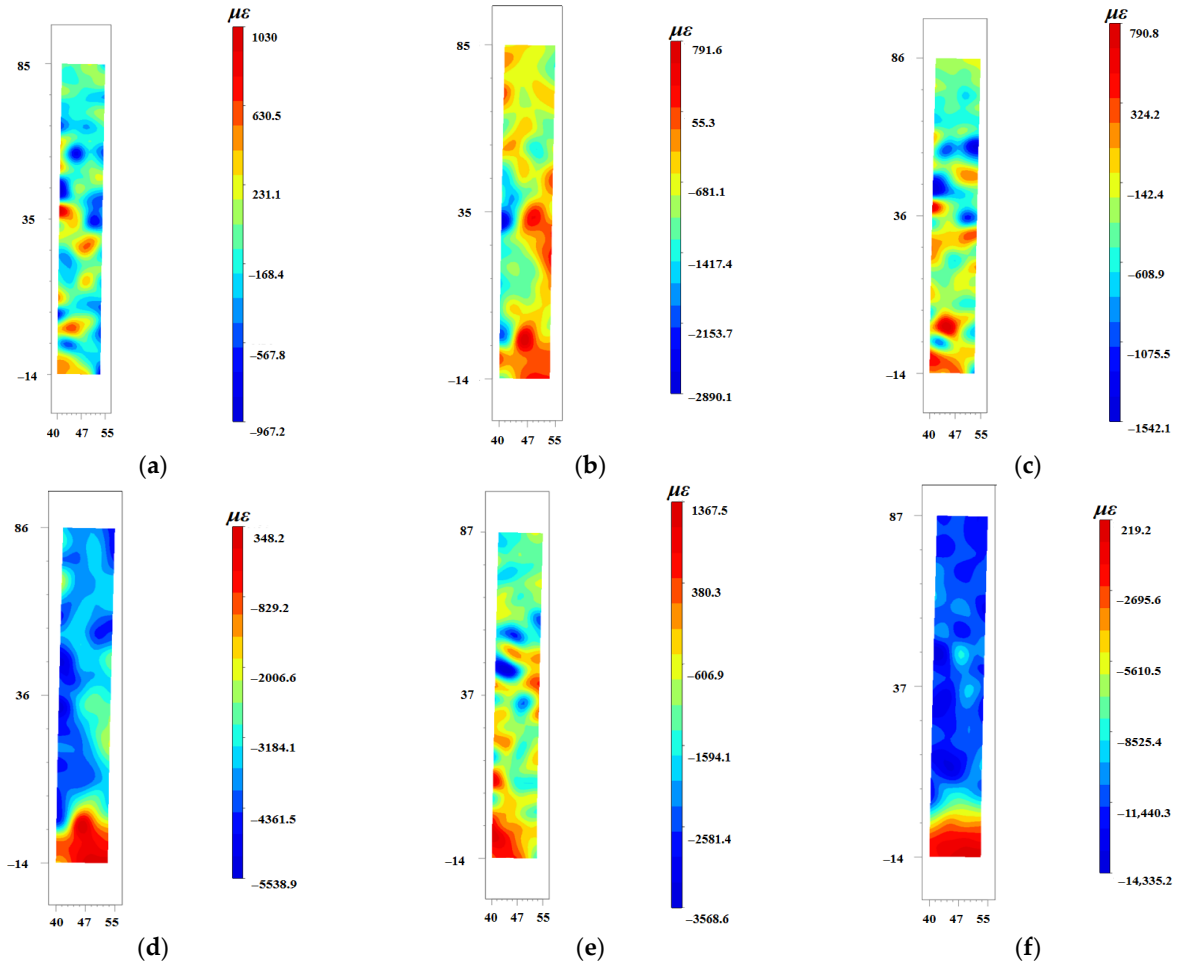

Figure 10. Surface strain cloud maps of test specimen: (**a**) Elastic stage eyy; (**b**) Elastic stage exx; (**c**) Yield stage eyy; (**d**) Yield stage exx; (**e**) Strain hardening stage eyy; (**f**) Strain hardening stage exx.

3.2. Test Specimen

Based on prior research, the corresponding dimensions of the test specimens were determined. The S-BRB utilized in the experimental studies incorporated a variable-section core plate with a total length of 1528 mm, a minimum width of 68 mm, a wedge ratio of 0.022, and a thickness of 6 mm. The restraining plate measured 6 mm in length, 80 mm in width, and 20 mm in thickness. Two limiting plates were installed within the energy-dissipating section of the core plate; each had a length of 80 mm, a width of 20 mm, and a thickness of 6 mm. These limiting plates effectively divided the core plate into three distinct sections with lengths of 515 mm, 486 mm, and 515 mm, respectively. The upper and lower restraining members were designed with a length of 1205 mm, a width of 108 mm, and a thickness of 6 mm. The lateral restraining members at both ends featured a length of 351 mm, a width of 100 mm, and a thickness of 8 mm, while the central lateral restraining member measured 481 mm in length, 100 mm in width, and 8 mm in thickness. All restraining members were assembled using high-strength bolts. The dimensional parameters of the S-BRB are illustrated in Figure 11. In addition, to preclude the transfer of shear forces between the core plate and the lateral restraining members, a clearance gap d was provided; accordingly, a 1 mm gap was maintained between the core plate and the lateral restraining members [34], whereas a 5 mm gap was reserved between the core plate and the restraining plates themselves. The test setup utilized an actuator to apply cyclic loads to the specimen, which was securely mounted on a robust loading frame to ensure stable support. The S-BRB, serving as the key component under investigation,

was connected to the floor girder within the structural assembly. The overall installation configuration is illustrated in Figure 12.

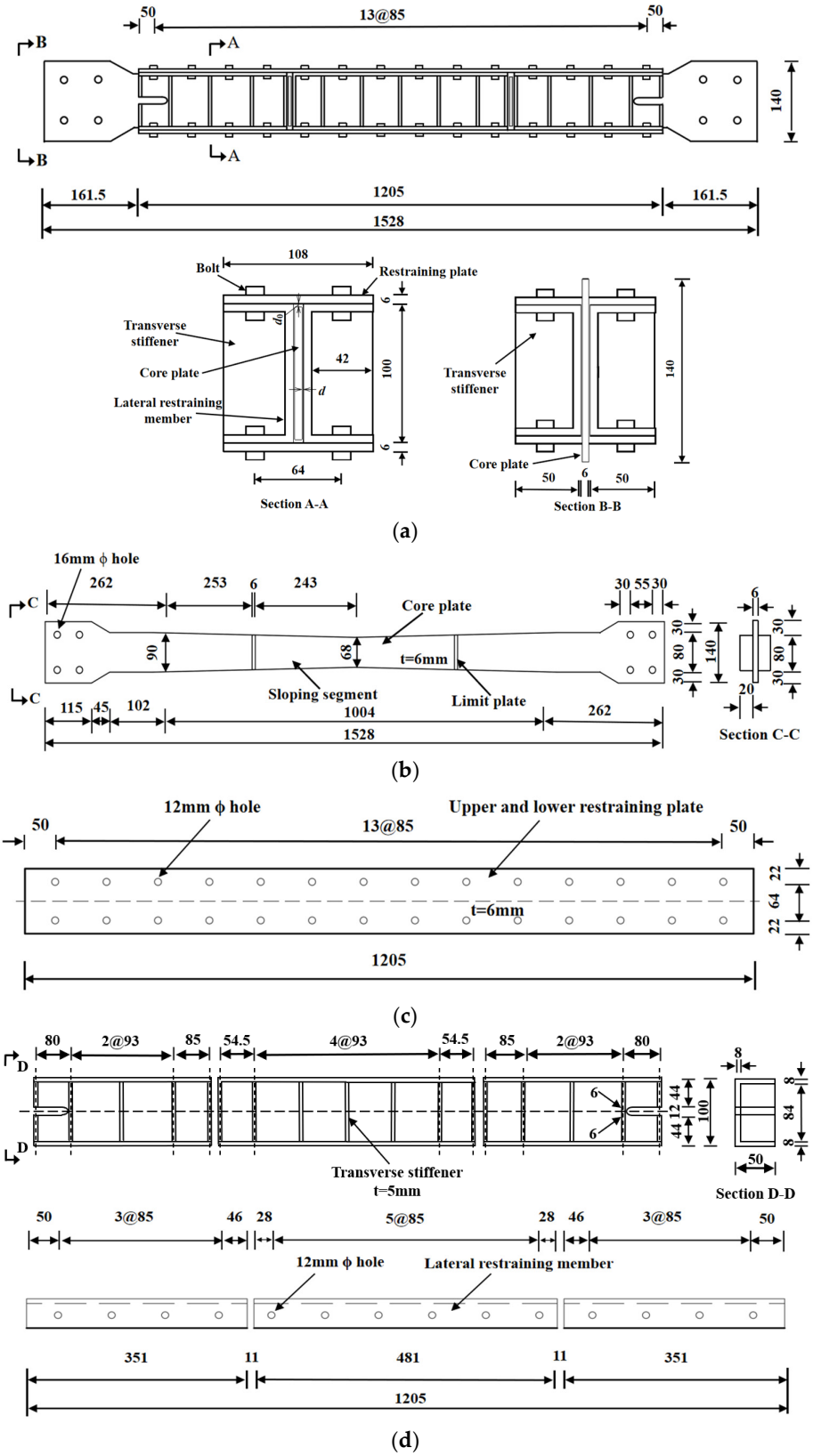

Figure 11. Dimension parameters of S-BRB: (**a**) front view; (**b**) core plate; (**c**) restraining plate; (**d**) lateral restraining member. (d = 1, gap between the core plate and lateral restraining member; d_0 = 5, gap between the core plate and the restraining plate).

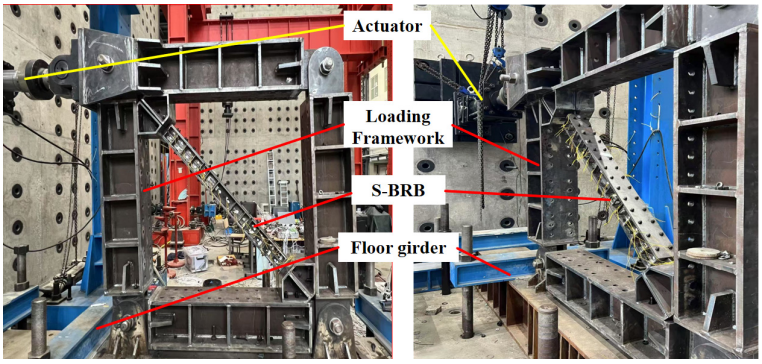

(**a**) (**b**)

Figure 12. Test setup of S-BRB: (**a**) Front view; (**b**) Side view.

To comprehensively monitor the deformation characteristics of the core plate, it was divided longitudinally into three sections: left, middle, and right. Each section was equipped with two measurement points to monitor strain development during loading, as depicted in Figure 13a. For the lateral restraining member, the core plate was similarly divided into three sections. Two measurement points were arranged in each of the left and right sections. Given the concentrated loading and complex deformation in the middle section, an increased number of measurement points were deployed to more accurately capture the strain distribution characteristics in this region, as shown in Figure 13b. All measurement points utilized high-precision strain gauges, and strain data were recorded in real-time via a data acquisition system, as illustrated in Figure 14.

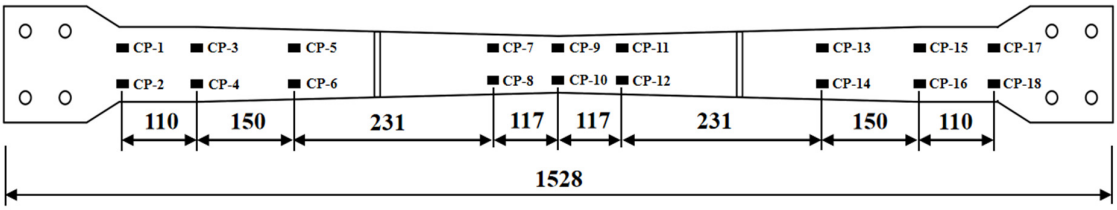

(**a**)

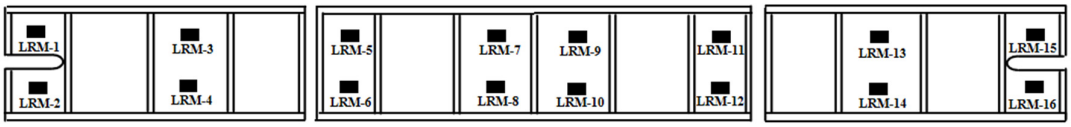

(**b**)

Figure 13. Strain-measurement points of the specimen: (**a**) Core plate; (**b**) Lateral restraining member.

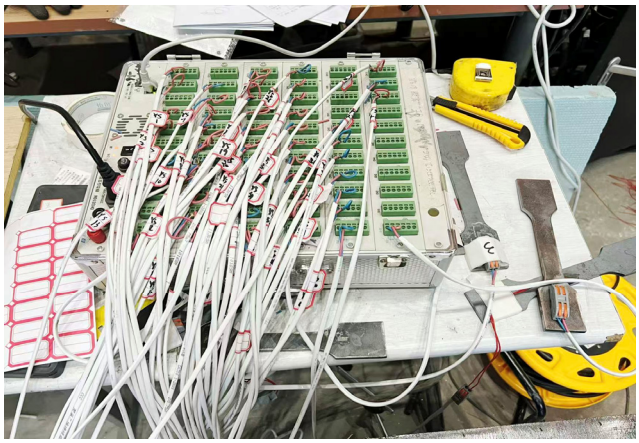

Figure 14. Static strain gauge.

3.3. Test Setup and Loading Protocol

In this study, the displacement control method was adopted for loading, with the specific loading program detailed in Figure 15. After first completing a pre-loading check, the formal test commenced, following a sequence of tension followed by compression. Specifically, three fully reversed cycles were applied at each of the following drift levels: 1/300, 1/200, 1/150, 1/100 and 1/50 of the total BRB length, as detailed in Table 1.

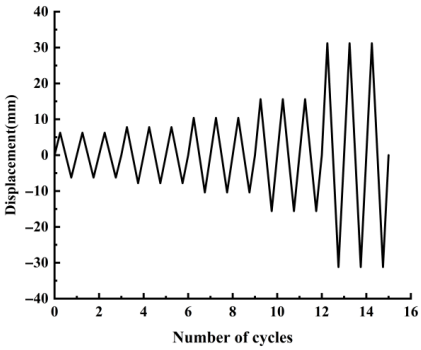

Figure 15. Loading program for specimen.

Table 1. Loading program.

Length of BRB/mm	Step	Cycle Times	Displacement/mm
1528	1~12	3	5.1 (L/300)
	13~24	3	7.6 (L/200)
	25~36	3	10.1 (L/150)
	37~60	3	15.3 (L/100)
	61~72	3	31.5 (L/50)

4. Test Results

During the initial stage of the test, the S-BRB was loaded with a displacement of 5.1 mm (L/300). After three complete loading cycles, the specimen remained in the elastic state with no observable surface changes. As loading progressed, a brief metallic clanging sound was heard from the buckling restrained brace end when the first compression displacement reached 7.6 mm (L/200). When the tensile displacement reached 10.1 mm (L/150), this sound weakened and transitioned into a slight friction noise. During the first displacement loading to 15.3 mm (L/100), intermittent metallic collision sounds were observed during both compression and tension cycles. By the second loading at this displacement, slight bending deformation was evident at the buckling restrained brace core plate end. Upon reaching a loading displacement of 31.5 mm (L/50) during the third cycle, the end of the core plate—specifically at the location lacking lateral restraining members—suddenly fractured, accompanied by distinct structural failure sounds. The test was terminated after unloading and applying reverse loading. The failure patterns of the core plate and an overall view of the specimen failure are shown in Figures 16 and 17.

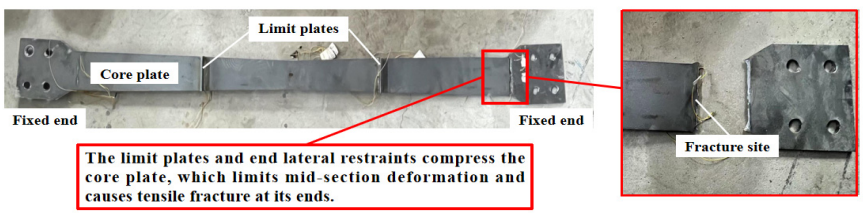

Figure 16. Failure mode of core plate.

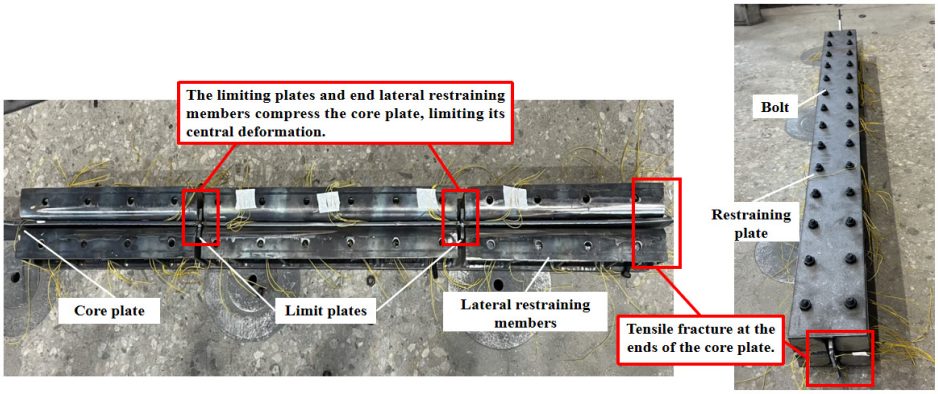

Figure 17. Overall view of specimen failure.

It is noteworthy that the primary failure occurred near the instrument loading end. Throughout the test, the limiting plate effectively protected the central region of the core plate, preventing excessive deformation concentration and ensuring that all parts of the core plate contributed fully to energy dissipation. The lateral restraining members and restraining plate, connected by bolts, formed a rigid frame system that provided continuous and reliable protection to the core plate. Under alternating tensile and compressive loads, the extended segment experienced fatigue failure before other regions, leading to buckling and fracture at its end. This configuration effectively delayed premature buckling instability and facilitated a segmented, progressive buckling and energy dissipation mechanism.

The cyclic response of the S-BRB, characterized by the hysteresis loop in Figure 18, demonstrates excellent energy dissipation. The full, symmetrical, and stable loops show negligible pinching and minimal degradation, as evidenced by the overlapping curves at identical displacements. After initial linear elastic behavior, the system sustained significant plastic deformation until fracture of the core plate at 31.2 mm terminated the test. The stabilization of the hysteresis loop area prior to failure underscores the robust cyclic performance and high ductility of the specimen.

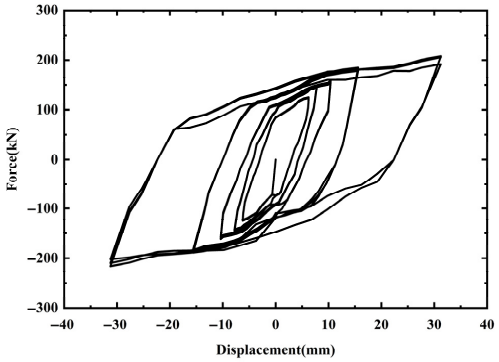

Figure 18. The hysteretic curve of test.

Figure 19 depicts the skeleton curve, characterizing the S-BRB's strength progression from linear elasticity (up to 10.1 mm) to a nonlinear plateau, achieving a peak capacity of 208.6 kN at approximately 20 mm. The failure of the core plate at 31.2 mm terminated the test, causing a drop in capacity. The energy dissipation performance was evaluated via the equivalent viscous damping ratio, calculated for the final cycle (considering asymmetric hysteresis) as per Equations (8)–(10) and Figure 19. The resulting values, summarized in Table 2, confirm the specimen's high damping capability.

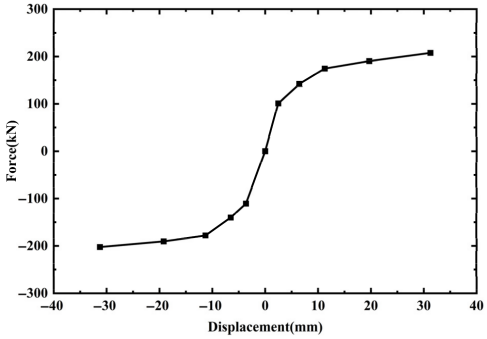

Figure 19. The skeleton curve of test.

Table 2. Seismic performance parameters of the test.

Hysteresis Loop	$\sum_{i=1}^{n}\left(E_i^+ + E_i^-\right)$ (kN·m)	ζ_{eq}	ζ_{eq}^+	ζ_{eq}^-
1	1.2	0.248	0.260	0.235
2	2.5	0.253	0.260	0.245
3	3.7	0.254	0.260	0.247
4	5.6	0.269	0.276	0.262
5	7.6	0.270	0.276	0.264
6	9.5	0.271	0.276	0.266
7	12.5	0.288	0.292	0.284
8	15.5	0.287	0.291	0.284
9	18.4	0.290	0.297	0.284
10	24.5	0.338	0.354	0.322
11	30.7	0.337	0.352	0.322
12	36.7	0.341	0.361	0.322
13	51.4	0.304	0.307	0.301
14	66.6	0.306	0.307	0.305
15	81.2	0.307	0.307	0.306

The equivalent viscous damping ratio, based on the principle of equal energy dissipation, serves as an indicator of energy absorption capability. Considering the tension-compression asymmetry, the entire loop along with the upper and lower half-loops of the last hysteretic cycle were selected [35]. The equivalent viscous damping ratio was calculated according to Equations (8)–(10) and the method illustrated in Figure 20. The results of these calculations are summarized in Table 2.

$$\zeta_{eq} = \frac{1}{2\pi}\frac{S_{ABC} + S_{ADC}}{S_{\Delta O'BE} + S_{\Delta O'DF}} \text{ (the entire loop)} \tag{8}$$

$$\zeta_{eq}^{+} = \frac{1}{2\pi}\frac{S_{ABC}}{S_{\Delta O'BE}} \text{ (upper half loop)} \tag{9}$$

$$\zeta_{eq}^{-} = \frac{1}{2\pi}\frac{S_{ADC}}{S_{\Delta O'DF}} \text{ (lower half loop)} \tag{10}$$

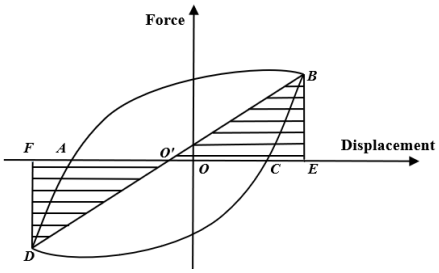

Figure 20. Calculation of equivalent viscous damping ratio.

The strain response of the S-BRB, detailed in Figures 21 and 22, demonstrates a distinct strain redistribution mechanism. The core plate strains evolve from a uniform elastic state to a yielded condition at the center, culminating in strain localization at the ends prior to fracture. This indicates a progressive shift in the force-resisting mechanism as damage accumulates. Conversely, the lateral restraining members exhibit minimal, purely elastic strain, confirming their effective confinement of the core plate.

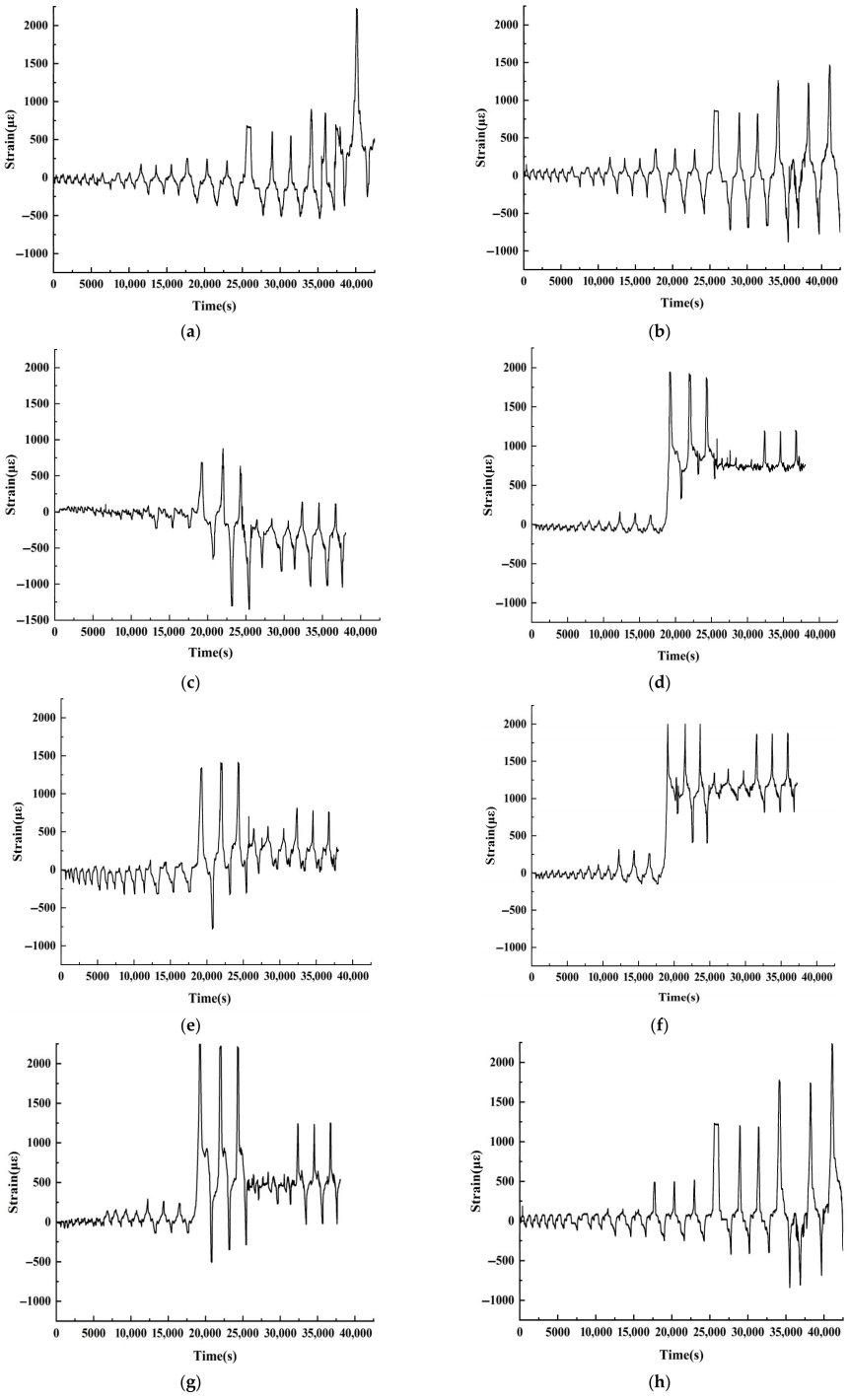

Figure 21. Strain changes at different positions on the core plate: (**a**) CP-1; (**b**) CP-4; (**c**) CP-5; (**d**) CP-7; (**e**) CP-9; (**f**) CP-11; (**g**) CP-13; (**h**) CP-16.

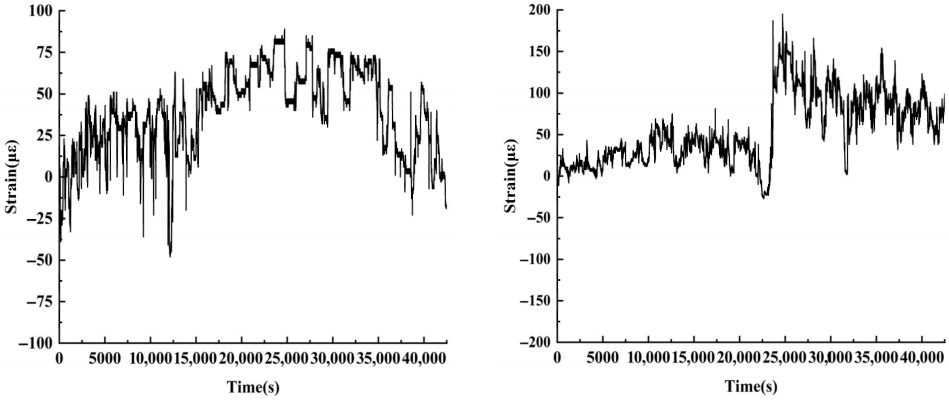

Figure 22. Strain changes at different positions on the lateral restraining members: (**a**) LRM-1; (**b**) LRM-16.

5. Numerical Analysis

5.1. Finite Element Modeling

The S-BRB numerical model was constructed using the same geometric and material parameters as the tested specimen, as detailed in Figure 11. The finite element model (FEM) included an accurate geometric representation of the bolts. In ABAQUS finite element analysis, the choice of solid element type and mesh size significantly impacts the accuracy, computational efficiency, and stability of model results [36]. This summary is based on our review of commonly used ABAQUS solid elements from relevant research as shown in Table 3. As the prevalence of interaction simulations within the models discussed in this paper, the C3D8R element is more suitable for selection.

Table 3. Comparisons of different 3D element type.

Type	Advantages	Disadvantages
C3D8: An 8-node linear brick.	Suitable for regular-shaped elements, enabling precise integration of polynomials within the stiffness matrix.	Risk of shear locking under bending loads, resulting in overestimated stiffness calculations.
C3D8R: An 8-node linear brick, reduced integration, hourglass control.	One fewer integration point per direction than fully integral elements, offering computational efficiency and superior adaptability to bending problems with reduced susceptibility to shear locking.	Sensitive to hourglass, potentially yielding excessively soft results.
C3D8I: An 8-node linear brick, incompatible modes.	Overcomes shear locking by introducing additional degrees of freedom, achieves accuracy close to quadratic elements, and has lower computational cost.	Sensitive to element distortion; unsuitable for contact analysis or large deformation problems.

The Chaboche constitutive model was adopted to calibrate the key parameters of the cyclic behavior, which was used to predict the hysteretic response of the steel [37]. The obtained material parameters were input into the model of the finite element software ABAQUS 2022 [38]. The material parameters in Table 4 can be used to provide a reference for simulating stress characteristics, and the criteria for isotropic hardening and kinematic hardening of the model are illustrated in Figure 23. In the isotropic hardening model, the yield surface stress σ_0 was a function of the equivalent plastic strain, and its relation was the stress when the equivalent plastic strain was zero, Q_∞ was the maximum change in the yield surface, and b was the index of the change in the yield surface. The back stress α in the kinematic hardening model was a function of the plastic strain ε_p. These material parameters were subsequently input into the finite element software ABAQUS to simulate the experimental hysteretic curves [36].

Table 4. Calibration parameters of specimens [38].

Specimen	Q_∞/MPa	$\sigma\|_0$/MPa	b	$C_{k,1}$/MPa	γ_1	$C_{k,2}$/MPa	γ_2	$C_{k,3}$/MPa	γ_3	$C_{k,4}$/MPa	γ_4
Average value	21	380	1.2	6013	173	5024	120	3026	32	990	35

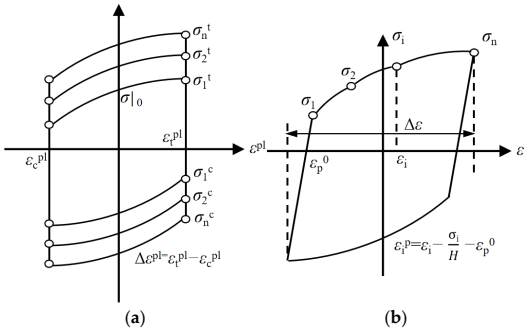

Figure 23. Plastic constitutive model proposed by Chaboche [37]: (**a**) isotropic hardening; (**b**) kinematic hardening.

To accurately replicate the actual boundary and loading conditions experienced by the S-BRB during testing, the loading frame was also explicitly modeled in ABAQUS. The finite element model of the S-BRB system is shown in Figure 24. The beams and columns of the loading frame were assumed to be connected with pinned joints. During the loading test, no bolt failure was observed; the test was terminated following core plate fracture. Bolt loads were accounted for in the ABAQUS simulation, with stresses remaining within the elastic range throughout the loading step. Consequently, damage initiation criteria were not considered. Within the ABAQUS simulations, lateral constraint elements of the BRB were assumed to be in surface-to-surface contact with both upper and lower constraint elements, as well as with the bolts. Friction between the core plate and restraining members was considered by using surface-to-surface contact, and the coefficient of friction was set to 0.3. Due to the current limitations in numerical strategies for predicting unstable crack propagation in bolted connections, the FEM did not incorporate damage or fracture mechanisms.

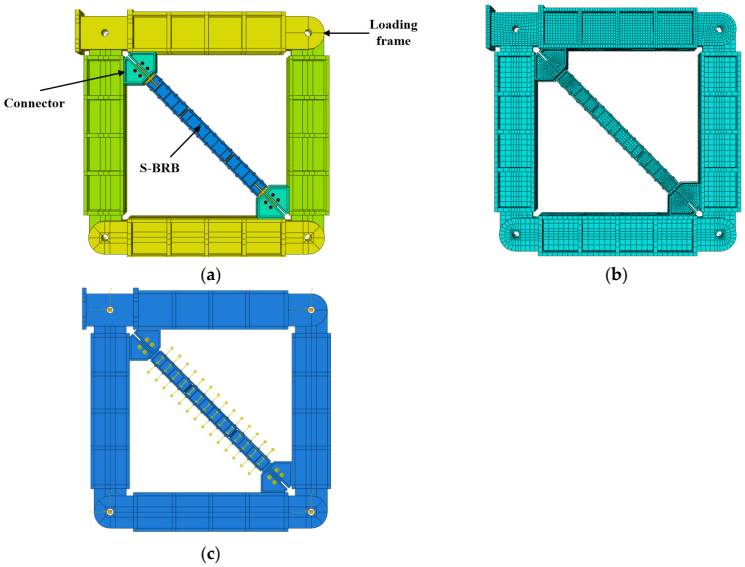

Figure 24. Finite element model of S-BRB: (**a**) Front view; (**b**) Model mesh; (**c**) Bolt load.

5.2. Mesh Sensitivity Analysis

A mesh sensitivity analysis was conducted to evaluate its influence on the BRB simulation, employing core plate element sizes of 9 mm, 12 mm, and 15 mm (Figure 25).

While the hysteresis loops for all models exhibited similar overall trends, the computed load-bearing capacity increased with larger mesh sizes (Figure 26). Given this sensitivity and the acceptable computational cost of the finer mesh (Table 5), the 9 mm model was selected for all subsequent analyses to ensure simulation accuracy.

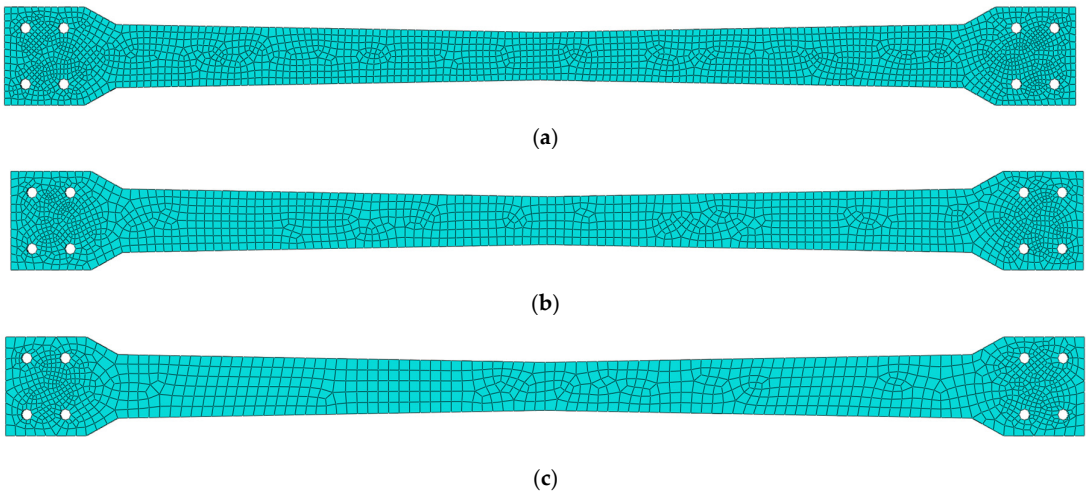

(**a**)

(**b**)

(**c**)

Figure 25. Different mesh model of core plate: (**a**) 9 mm; (**b**) 12 mm; (**c**)15 mm.

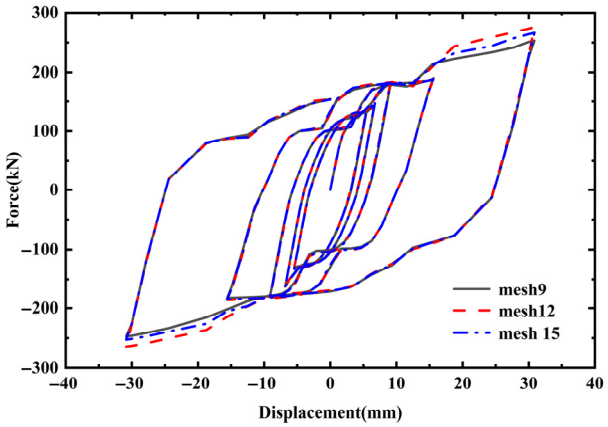

Figure 26. The hysteretic curves of simulation with different mesh.

Table 5. Comparison of computational efficiency.

Mesh Size	Total Number of Elements	Runtime
9 mm	123822	14 h
12 mm	102124	13.5 h
15 mm	84962	13 h

5.3. Imperfection Sensitivity Analysis

Different imperfection amplitudes (L/1000, L/300) were considered in this section as shown in Figure 27. The influence of initial geometric imperfections was included by superimposing the first-order buckling mode. Comparing the simulated hysteresis curve results under different initial conditions reveals that as the initial defect increases, the envelope area of the BRB hysteresis curve decreases, and the peak load of the BRB is reduced. The comparative analysis demonstrates that the BRB's performance is highly sensitive to initial geometric imperfections, underscoring the necessity for strict fabrication tolerances.

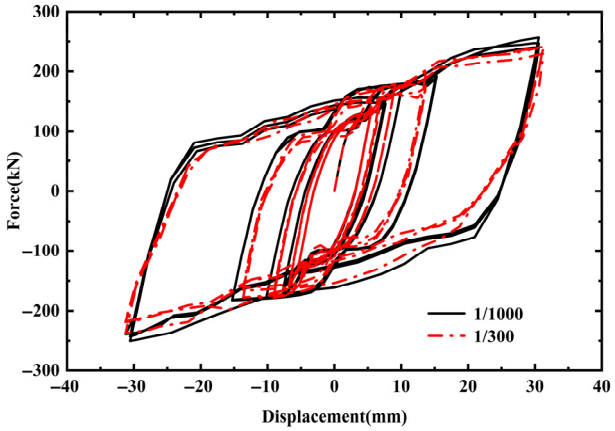

Figure 27. The hysteretic curves of simulation with different imperfection amplitudes.

5.4. Numerical Analysis Results

A comparison between the finite element simulation and the experimental hysteresis curves of the S-BRB is presented in Figure 28. The results indicate that the hysteresis curve obtained from the finite element simulation is more fully developed than its experimental counterpart. This discrepancy may be attributed to insufficient bolt preload during the experiment, which could have resulted in slippage that was not accounted for in the numerical model. Consequently, the simulated hysteresis loops exhibit a more complete and stable shape. Overall, however, the peak load points in each cycle show a high degree of agreement between the experimental and numerical results, and the general trends are consistent.

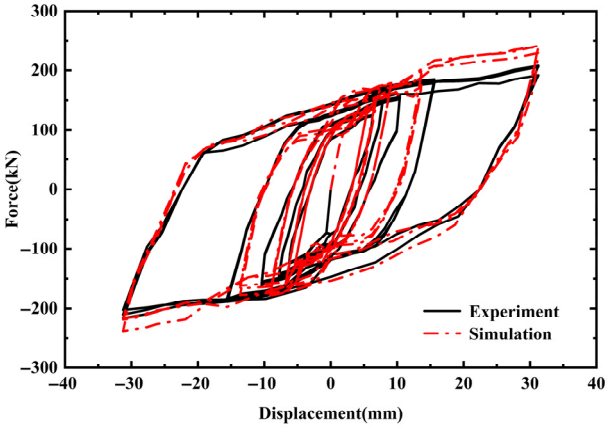

Figure 28. The hysteretic curves of experiment and simulation.

The skeleton curves derived from the finite element simulation and the experimental data are compared in Figure 29. Due to the fracture of the core plate in the test, the experimental specimen experienced a rapid decrease in load-bearing capacity. As a result, the finite element model, which did not include fracture, predicted higher ultimate loads. Under positive loading, the simulated maximum load-bearing capacity was 248.63 kN, compared to the experimental value of 225.65 kN. Under negative loading, the simulated capacity was −237.42 kN, while the experimental result was −218.35 kN. The difference between the simulated and experimental maximum loads was approximately 10.2%, which may be attributed to factors such as slippage in the physical loading device. A comparison of the equivalent viscous damping ratios validates the numerical model, as the simulated values show close alignment with experimental results (Table 6). This confirms the model's efficacy in replicating the key energy dissipation performance of the S-BRB.

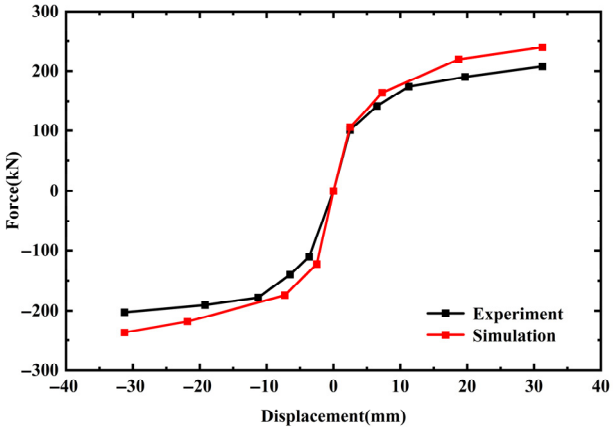

Figure 29. The skeleton curves of experiment and simulation.

Table 6. Comparison of equivalent viscous damping ratio.

Hysteresis Loop	Experiment	Simulation
1	0.248	0.260
2	0.253	0.286
3	0.254	0.285
4	0.269	0.274
5	0.270	0.277
6	0.271	0.276
7	0.288	0.293
8	0.287	0.296
9	0.290	0.294
10	0.338	0.339
11	0.337	0.345
12	0.341	0.343
13	0.304	0.320
14	0.306	0.308
15	0.307	0.315

The lateral deformation of the core plate and the lateral constraint elements under cyclic loading is illustrated in Figure 30. In conventional constant-section buckling-restrained braces, the ends of the core plate are typically subjected to higher local compressive stresses than the central region, leading to premature local buckling failure at the ends. The stress distribution and plastic equivalent strain obtained from the numerical model are shown in Figures 31 and 32, respectively. The maximum stress occurred at the ends of the two limiting plates, confirming their effective function. Figure 32 reveals that equivalent plastic strain is concentrated in the central region and at the ends of the core plate. This indicates that these areas dissipated a significant amount of energy during the loading process.

With the assistance of these limiting plates, the deformation of the core plate was distributed over a larger area, allowing each segment to contribute more uniformly to load-bearing and energy dissipation. This design significantly reduces the risk of sudden failure in the central region of the core plate, thereby enhancing the stability and durability of the entire buckling restrained brace system under cyclic loading.

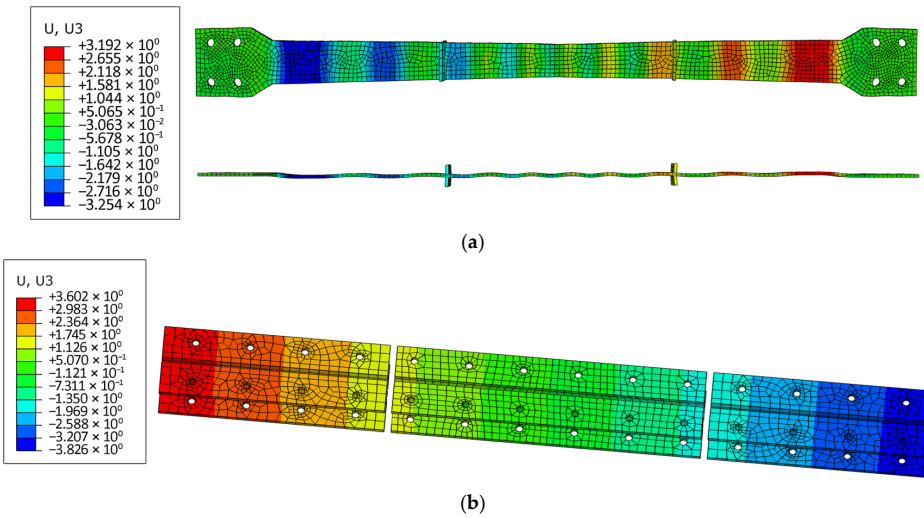

Figure 30. The lateral deformation of the model: (**a**) Core plate; (**b**) Lateral restraining members. (unit: mm).

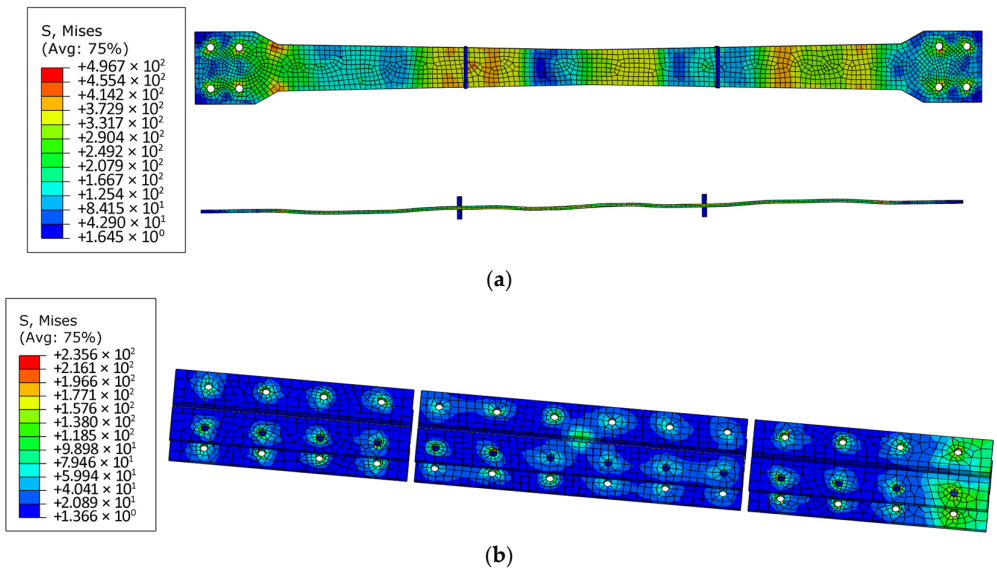

Figure 31. The stress distribution of the model: (**a**) Core plate; (**b**) Lateral restraining members. (unit: MPa).

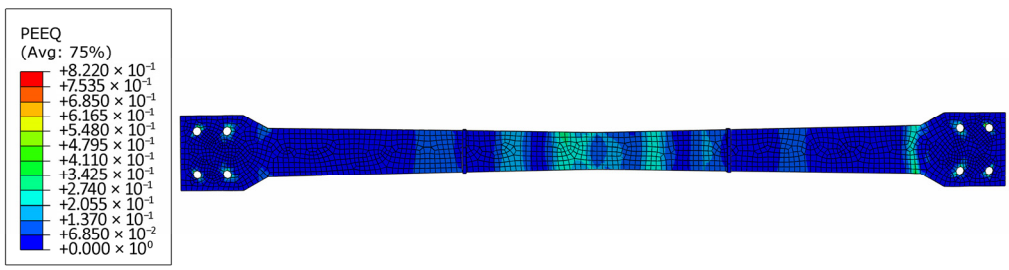

Figure 32. The plastic equivalent strain distribution of the model.

Furthermore, the stresses in the lateral constraint components remained relatively low and well below the yield stress, indicating that these elements stayed within the elastic range throughout the loading process. These components play a critical role in restraining the lateral deformation of the core plate. The finite element analysis results are highly consistent with the experimental failure modes, which validates the accuracy of the numerical model and confirms the reliability of the experimental methodology.

6. Conclusions

This study systematically investigated the seismic performance of the segmented buckling-restrained brace (S-BRB) through theoretical analysis, experimental testing, and numerical simulation. The main conclusions are as follows:

Through a variable cross-section design of the core plate and rational arrangement of the limiting plates, the S-BRB achieves a segmented yielding and energy dissipation mechanism. This design effectively prevents the premature failure at the weakest section commonly seen in conventional BRBs, thereby significantly enhancing the overall seismic performance.

The quasi-static test results demonstrated that the S-BRB exhibits stable, symmetric, and full hysteretic loops under cyclic loading, with no significant pinching effect observed. This indicates excellent energy dissipation and deformation capacity. Although fracture eventually occurred at the end of the core plate due to stress concentration, the central region remained protected by the limiting plates without excessive deformation, which validates the effectiveness of the segmented energy dissipation mechanism.

Furthermore, numerical simulation results showed good agreement with the experimental data, confirming the accuracy of the established ABAQUS model. Finite element analysis further revealed the interaction mechanism between the core plate and lateral restraining members. The limiting plates effectively distribute plastic deformation, prevent local instability, and improve the overall stability of the system.

The all-bolted connections and modularity of the S-BRB enhance constructability and facilitate post-earthquake repair, contributing to favorable lifecycle economic efficiency. However, the absence of specific provisions in current seismic design codes presents a barrier to widespread adoption. This study provides a foundational experimental and theoretical basis for the S-BRB system. To transition this technology to practice, future research should focus on optimizing key details—such as the configuration of limiting plates and the profile of the variable-cross-section core—through testing of large-scale specimens and sub-structures. These efforts are critical to establishing robust design guidelines and fully validating the system's scalability and cost-effectiveness.

Author Contributions: Conceptualization, S.X. and Y.L. (Yanyan Liu); methodology, X.W.; software, S.X. and Y.Y.; formal analysis, W.W.; investigation, Y.Y.; resources, Y.L. (Yan Li); data curation, X.W.; writing—original draft preparation, S.X. and Y.Y.; writing—review and editing, S.X. and Y.L. (Yanyan Liu); visualization, W.W.; supervision, S.X.; funding acquisition, S.X. All authors have read and agreed to the published version of the manuscript.

Funding: This research was funded by Science and Technology Development Plan Project of Jilin Province, China, grant number YDZJ202401594ZYTS and The APC was funded by Shuai Xu.

Data Availability Statement: The data used to support the findings of this study are available from the corresponding author upon request.

Conflicts of Interest: The authors declare no conflicts of interest.

References

1. Suzuki, A.; Ohno, S.; Kimura, Y. Risk Assessment of Overturning of Freestanding Non-Structural Building Contents in Buckling-Restrained Braced Frames. *Buildings* **2024**, *14*, 3195. [CrossRef]
2. Zhang, C.; Guo, X.; Zhao, Y.; Liu, Y. Development of an innovative assembled self-centering dual-stage yield buckling-restrained brace for improving seismic resilience. *Eng. Struct.* **2025**, *329*, 119804. [CrossRef]
3. Kato, S.; Takiuchi, Y.; Abe, K.; Mukaiyama, Y.; Nakazawa, S. Effectiveness of buckling restrained braces for upgrading earthquake resistant capacity of single layer grid dome. *Eng. Struct.* **2022**, *261*, 114280. [CrossRef]
4. Carofilis, W.; Kim, E.K.; Jung, D. Seismic loss and resilience assessment of a steel building retrofitted with self-centering buckling-restrained braces. *Earthq. Spectra* **2025**, *41*, 1689–1712. [CrossRef]

5. Capacci, L.; Lago, D.B. Structural modelling and probabilistic seismic assessment of existing long-span precast industrial buildings. *Bull. Earthq. Eng.* **2025**, *23*, 2581–2609. [CrossRef]
6. Shi, S.; Xin, L.; Huang, C.; Han, G.; Xu, Z.; Chen, X. Seismic retrofit of high-rise buildings using buckling-restrained braces: Design methodology and performance evaluation. *Sci. Rep.* **2025**, *15*, 27546. [CrossRef]
7. Talukdar, D.; Sen, K.M.; Chakravarty, S. Comprehensive Seismic Analysis and Design Strategies for Enhanced Building Resilience: A Comparative Study of Regular and Irregular Structures. *J. Inst. Eng. Ser. A* **2024**, *106*, 329–345. [CrossRef]
8. Akrivi, C.; Dimitrios, V.; Enrique, M.H. Performance-based versus conventional seismic design: Comparative assessment on a 4-story RC moment frame. *Bull. Earthq. Eng.* **2024**, *22*, 3031–3053. [CrossRef]
9. Lia, P.; Li, H.; Zhang, T.; Chen, G.; He, Y.; Li, Z.; Xiong, G. Experimental investigation and numerical study of all-steel buckling-restrained braces. *Structures* **2025**, *77*, 109228. [CrossRef]
10. Hoveidae, N.; Rafezy, B. Overall buckling behavior of all-steel buckling restrained braces. *J. Constr. Steel Res.* **2012**, *79*, 151–158. [CrossRef]
11. Yin, L.; Zhu, Y.; Cai, X.; Xu, Z.; Zhang, J. Seismic performance of self-centering precast concrete buckling-restrained braced frame sub-assembly. *J. Build. Eng.* **2025**, *107*, 112690. [CrossRef]
12. Wu, K.; Wei, G.; Zhang, L.; Yu, W.; Lan, X. Experimental Study on the Seismic Behavior of All-Steel Buckling-Restrained Braces Without an Unbonded Material Layer. *Buildings* **2025**, *15*, 1626. [CrossRef]
13. Wang, M.; Tong, Y. Experimental study on seismic performance of assembled buckling-restrained brace with low yield point steel. *Thin-Walled Struct.* **2024**, *205*, 112474. [CrossRef]
14. Serin, B.; Bozkurt, B.M. Development of replaceable core all-steel buckling-restrained braces. *J. Constr. Steel Res.* **2025**, *226*, 109247. [CrossRef]
15. Chen, H.; Bai, J.; Liu, J. Development of earthquake-resilient precast concrete beam-to-column connections with bottom replaceable buckling-restrained brace dampers. *Eng. Struct.* **2025**, *339*, 120660. [CrossRef]
16. Kuwahara, S.; Tada, M.; Yoneyama, T.; Imai, K. A study on stiffening capacity of double-tube members. *J. Struct. Constr. Eng.* **1993**, *445*, 151–158.
17. Genna, F.; Gelfi, P. Analysis of the lateral thrust in bolted steel Buckling-Restrained Braces. I: Experimental and numerical results. *J. Struct. Eng.* **2012**, *138*, 1231–1243. [CrossRef]
18. Usami, T.; Wang, C.L.; Funayama, J. Developing high-performance aluminum alloy buckling-restrained braces based on series of low-cycle fatigue tests. *Earthq. Eng. Struct. Dyn.* **2012**, *41*, 643–661. [CrossRef]
19. Hoveidae, N.; Radpour, S. A novel all-steel buckling restrained brace for seismic drift mitigation of steel frames. *Bull. Earthq. Eng.* **2021**, *19*, 1537–1567. [CrossRef]
20. Zhou, Y.; Cao, Y.; Takagi, J.; Zhong, G.; He, Z. Experimental and numerical investigation of a novel all-steel assembled core-perforated buckling-restrained brace. *J. Constr. Steel Res.* **2022**, *193*, 107288.
21. Jiang, Z.; Guo, Y.; Zhang, A.; Dou, C.; Zhang, C.-X. Experimental study of the pinned double rectangular tube assembled buckling-restrained brace. *J. Zhejiang Univ. Sci. A* **2017**, *18*, 20–32. [CrossRef]
22. Jia, L.; Ge, H.; Maruyama, R.; Shinohara, K. Development of a novel high-performance all-steel fish-bone shaped buckling-restrained brace. *Eng. Struct.* **2017**, *138*, 105–119. [CrossRef]
23. Azizi, H.; Ahmadi, J. Mitigation of residual deformations in steel braced frames through an innovative Y-shaped hybrid buckling restrained braces. *J. Constr. Steel Res.* **2025**, *229*, 109533. [CrossRef]
24. Hu, B.; Shi, W.; Hu, R.; Xia, W.; Man, H. The experimental research of a new fabricated buckling restrained brace. *Earthq. Eng. Eng. Vib.* **2015**, *35*, 132–136. (In Chinese)
25. Ma, L.; Luo, X.; Ren, Y. Seismic performance analysis of reinforced multi-story frames with external fractal dimension-buckling restrained braces. *J. Asian Archit. Build. Eng.* **2025**, 1–17. [CrossRef]
26. Takeuchi, T.; Wada, A. Review of buckling-restrained brace design and application to tall buildings. *Int. J. High-Rise Build.* **2018**, *7*, 187–195.
27. Shrif, M.; Al-Sadoon, Z.A.; Habib, A. Seismic performance and configuration assessment of deficient steel frames equipped with buckling-restrained braces. *Civ. Eng. J.* **2024**, *13*, 198–217.
28. Bagheri, M.; Ranjbar Malidarreh, N.; Ghaseminejad, V.; Asgari, A. Seismic resilience assessment of RC superstructures on long–short combined piled raft foundations: 3D SSI modeling with pounding effects. *Structures* **2025**, *81*, 110176. [CrossRef]
29. Xu, S.; Li, L.; Wang, X. A Fully Bolted BRB and Its Preparation Method. CN113565228B, 14 February 2025.
30. Xu, S.; Hu, Y.; Yin, Y.; Guo, C. Hysteretic behavior of the segmented buckling-resistant braces with LYP160. *Eng. Rep.* **2024**, *6*, e12916. [CrossRef]
31. *GB/T 228.3-2019*; Metallic Materials—Tensile Testing—Part 3: Method of Test at Low Temperature. National Technical Committee for Steel of Standardization Administration of China. Standards Press of China: Beijing, China, 2019.
32. Zhao, J.; Yan, L.; Wang, C.; Zhou, Y.; Chen, R.; Chan, T.-M. Damage-control design and hybrid tests of a full-scale two-story buckling-restrained braced steel moment frame with sliding gusset connections. *Eng. Struct.* **2023**, *275*, 115263. [CrossRef]

33. Zhao, J.; Wu, B. Working mechanism and stability design method of buckling-restrained braces. *Earthq. Eng. Eng. Vib.* **2009**, *29*, 131–139.
34. *JGJ/T 101—2015*; Specification for Seismic Test of Buildings. Ministry of Housing and Urban-Rural Development of the People's Republic of China (MOHURD). China Architecture & Building Press: Beijing, China, 2015.
35. Clough, R.; Penzien, J. *Dynamics of Structures*; Computers & Structures, Inc.: Berkeley, CA, USA, 1995.
36. *ABAQUS Document Version 2022*; Dassault Systems: Paris, France, 2022.
37. Chaboche, J.L. Time-independent constitutive theories for cyclic plasticity. *Int. J. Plast.* **1986**, *2*, 149–188. [CrossRef]
38. Shi, Y.; Wang, M.; Wang, Y. Experimental study of structural steel constitutive relationship under cyclic loading. *J. Build. Mater.* **2012**, *15*, 293–300.